

# Study of dark counts in optical superconducting transition-edge sensors

Laura Manenti,<sup>1,2,\*</sup> Carlo Pepe,<sup>3,4,5</sup> Isaac Sarnoff,<sup>1,2,†</sup> Tengiz Ibrayev,<sup>1,2</sup> Panagiotis Oikonomou,<sup>1,2</sup> Artem Knyazev,<sup>1,2</sup> Eugenio Monticone,<sup>4</sup> Hobey Garrone,<sup>3,4</sup> Fiona Alder,<sup>6</sup> Osama Fawwaz,<sup>1,2</sup> Alexander J. Millar,<sup>7,8</sup> Knut Dundas Morå,<sup>9</sup> Hamad Shams,<sup>1,2</sup> Francesco Arneodo,<sup>1,2</sup> and Mauro Rajteri<sup>4</sup>

<sup>1</sup>*Division of Science, New York University Abu Dhabi, United Arab Emirates*

<sup>2</sup>*Center for Astrophysics and Space Science (CASS),*

*New York University Abu Dhabi, United Arab Emirates*

<sup>3</sup>*Dipartimento di Elettronica Telecomunicazioni Politecnico di Torino,*

*Corso Duca degli Abruzzi 24, 10129 Torino, Italy*

<sup>4</sup>*INRiM, Istituto Nazionale di Ricerca Metrologica, Strada delle Cacce, 91 – 10135 Torino, Italy*

<sup>5</sup>*INFN Sezione di Torino - Torino, Italy*

<sup>6</sup>*Dept. of Physics and Astronomy, University College London, Gower Street, London, United Kingdom*

<sup>7</sup>*Theoretical Physics Division, Fermi National Accelerator Laboratory, Batavia, IL 60510, USA*

<sup>8</sup>*Fermi National Accelerator Laboratory, Batavia, IL 60510, USA*

<sup>9</sup>*Physics Department, Columbia University, New York, New York 10027, USA*

(Dated: February 7, 2024)

Superconducting transition-edge sensors (TESs), known for their high single-photon detection efficiency and low background, are increasingly being used in rare event searches. We present the first comprehensive characterization of optical TES backgrounds, identifying three event types: high-energy, electrical noise, and photon-like events. We experimentally verify and simulate the source of the high-energy events. We develop an algorithm to isolate photon-like events, the expected signal in dark matter searches, achieving record-low photon-like dark count rates in the 0.8 to 3.2 eV energy range.

*Introduction.* In recent years, multilayer dielectric haloscopes have emerged as a promising method for the detection of dark photons (DP), a possible dark matter (DM) candidate [1]. The detection principle of a DP haloscope is as follows: a stack of dielectric bilayers converts dark photons from the local DM halo into Standard Model (SM) photons, then a lens focuses the converted photons onto a photosensor [2, 3]. Since the rest mass of the DP is entirely converted into the energy of the SM photon, the choice of the photosensor will determine the DP mass range the haloscope is sensitive to. Two experiments deployed this technology for the first time in 2021: LAMPOST [4], in the USA, and MuDHI [5], in the UAE. MuDHI operated a prototype detector at New York University Abu Dhabi (NYUAD) to search for DP in the mass range around 1.5 eV. A commercially available single-photon avalanche diode (SPAD) was used as the photosensor [6]. Although the SPAD could have in principle achieved a higher detection efficiency under optimal conditions ( $\sim 80\%$  at 800 nm as per the manufacturer’s data sheet), it exhibited a low detection efficiency ( $\sim 2\%$ ) when operated near the breakdown voltage, a trade-off needed to reduce the dark count rate (DCR). This DCR was around  $\sim 100$  Hz at temperatures below  $0^\circ\text{C}$  and when operating a few volts above the breakdown voltage. Having to compromise between high detection efficiency and low dark count rate notably reduces the detector’s overall sensitivity.

Quantum sensors, such as superconducting-nanowire

single-photon detectors (SNSPDs) used by LAMPOST, offer a significant advantage with their low dark count rate and sensitivity to single-photon energy depositions. A feature of SNSPDs, as well as SPADs, is that they function as an on/off detector [7], only indicating whether the detector has been struck by a particle without measuring its energy. Conversely, superconducting transition-edge sensors (TESs) are micro-calorimeters [8], whose signal is proportional to the energy deposited by a particle. This makes them our preferred choice as the photosensor in the dielectric haloscope as they can discriminate events by their energy.

The sensitivity of dielectric haloscopes and other rare event searches using TESs is mainly limited by the TES DCR. In this work, we measured the DCR of two optical TESs (i.e., TESs sensitive to photons in the optical range) and developed a set of experimental and data processing methods to characterize, reduce, and mitigate their background rate. Using these methods, we obtained a photon-like DCR (see below for the definition) of  $6 \times 10^{-5}$  Hz at  $1.5 \pm 0.2$  eV, the targeted range of MuDHI. This represents an improvement of approximately seven orders of magnitude compared to the SPAD. This advancement in reducing the DCR is crucial for the use of TESs in dielectric haloscopes and other rare event searches. Furthermore, we have identified and explained the primary contributors to optical TES dark counts for the first time, linking them to cosmic ray interactions with the TES substrate.

*Design and operating principle of TESs.* A TES is a thin superconducting film operated at the transition between its superconducting and normal state where it is most sensitive to changes in temperature. The TES

\* [laura.manenti@nyu.edu](mailto:laura.manenti@nyu.edu)

† [sarnoff@nyu.edu](mailto:sarnoff@nyu.edu)

working point is stabilized on the transition by negative electrothermal feedback [9] which is achieved by applying a voltage bias. This means that any increase in temperature (due to energy absorption) leads to an increase in resistance, which in turn causes a decrease in current. This drop in current reduces Joule heating, thereby cooling the sensor and bringing it back to the working point. A direct current superconducting quantum interference device (dc-SQUID) connected to the TES acts as a transimpedance amplifier [10]. It converts the current drop resulting from the particle interaction to a measurable voltage drop. This voltage can then be amplified by standard electronic amplifiers and the waveforms can be measured and recorded by an oscilloscope. The voltage drop produced by the dc-SQUID is proportional to the energy deposition in the TES [9].

The two superconducting TESs used in this work were fabricated and operated at the Istituto Nazionale di Ricerca Metrologica (INRiM) in Turin (Italy). They are made of a bilayer of titanium, the superconducting material, and gold, a normal metal to lower the critical temperature,  $T_c$ , of the titanium ( $\sim 400$  mK) by the proximity effect [11]. Both TESs exhibit a  $T_c$  of around 90 mK and were operated inside an adiabatic demagnetization refrigerator (ADR) with a base temperature of 30 mK. Since TESs and dc-SQUIDs are sensitive to magnetic fields, including the geomagnetic one, a cryogenic magnetic shield was installed within the ADR around the working area to suppress any magnetic interference that could degrade the sensor’s performance.

Two  $20 \times 20 \mu\text{m}^2$  TESs were deposited on silicon substrates. We refer to the sensors as “TES E” and “TES B.” Most of the data have been acquired from TES E, making it the primary focus of our study. Unless otherwise specified, references to TES data should be assumed to pertain to TES E. In the Supplemental Material [? ], we provide details on the TESs fabrication and some information about the characterization and dark count rate of TES B. For both TES E and TES B, the bath temperature was consistently maintained at 43 mK, with the working point set at 15% of their normal resistance.

*Calibration.* To calibrate the TES, we coupled it to three different attenuated monochromatic lasers of 1540 nm, 850 nm, and 406 nm using an optical fiber. The attenuation allows us to restrict the number of photons arriving onto the TES and avoid signal saturation, focusing on the 1–8 photon region. In Fig. 1, the calibration curve is shown on the right, where we plot the measured signal amplitude from the TES against the known energy of the impinging photon(s). The left side of the figure displays the histograms of counts versus amplitude for each laser wavelength used.

*Type of signal events.* Signals detected by the TES without any input optics are referred to as “intrinsic detector dark counts” by Ref. [7]. However, in this manuscript we drop the adjective “intrinsic” as we have identified external sources contributing to these counts

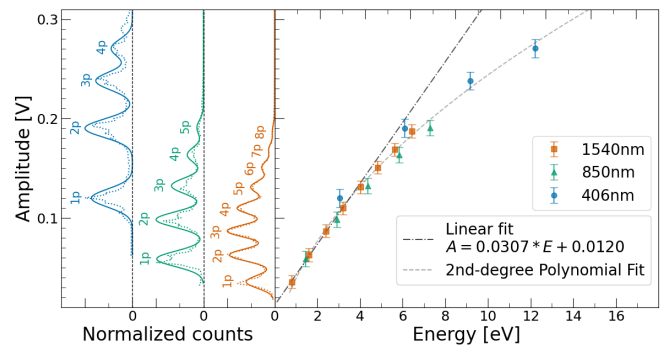


FIG. 1. Calibration of TES E using optically coupled, attenuated laser diodes. Right: The calibration curve, with signal amplitude (V) plotted against photon energy (eV). Data points are color-coded by laser wavelength: blue for 406 nm, green for 850 nm, and orange for 1540 nm. Left: Histograms showing count distribution versus amplitude for each wavelength. The total number of counts in each histogram is normalized to 100. A multi-Gaussian fit (solid line) is shown on top of the raw data (dotted line). Peaks correspond to different photon multiplicities at each wavelength, with their mean values aligning with the data points in the calibration plot. The TES response is linear from 0 to 5 eV, matching the TES’s operational range. Beyond 5 eV, the response becomes non-linear. For completeness, a second-degree polynomial fit to the full energy spectrum is also shown.

such that not all of the dark counts come from within the sensor (i.e., they are not intrinsic to it). The observed signals fall into three distinct categories: photon-like, high-energy, and electrical noise events. While the three kinds of pulses are visually distinguishable, we have automated the categorization using the following pipeline developed in Python. After applying a Butterworth filter, we calculate a set of variables for each waveform (e.g., full width at half maximum, maximum amplitude, pulse area, etc.). We employ principal component analysis (PCA) to find the two linear combinations of variables that maximize the variance of the points [12]. K-means clustering is then applied to the resulting 2D phase space to identify clusters of similar events [13]. To ensure the accuracy of this automated sorting, we conducted a manual review of the clusters.

This review process is facilitated by a graphical user interface (GUI) that allows for the selection of a cluster center, subsequently displaying all waveforms associated with that cluster for quick verification of classification. In some cases, as demonstrated in Fig. 2, it is necessary to reapply the clustering algorithm on a subset of the data to fully separate the three groups.

Photon-like events are the green points in group A in Fig. 2, which was obtained by rerunning the classification algorithm on clusters 8 and 9. These signals are characterized by a sharp rise time  $\lesssim 1 \mu\text{s}$  and look identical to the ones we see when we shine light from the attenuated laser diode onto the TES.

Signals in clusters 1–7 in Fig. 2 are characterized by

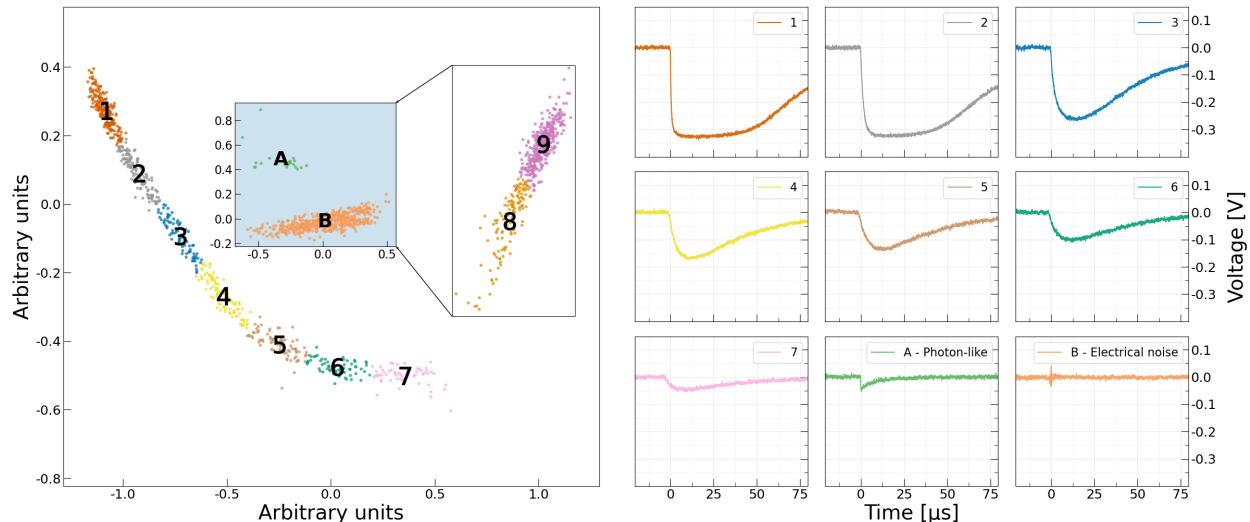


FIG. 2. Left panel: K-means clustering of signals from background run after principal component analysis. The inset zooms in on clusters 8 and 9, which were reanalyzed to improve the separation of noise from photon-like events. Right panel: Sample signal waveforms from each of the refined clusters.

a long rise and decay time, suggesting these events are caused by large energy depositions in the TES substrate, likely coming from primary or secondary cosmic ray particles or naturally occurring radioactive decays. We therefore refer to them as “high-energy events.” This classification is consistent with the observed long rise time, which can be attributed to the slow diffusion of energy from the substrate into the TES.

Electrical noise events (orange cluster B in Fig. 2 obtained by reanalyzing clusters 8 and 9) exhibit voltage spikes oscillating between positive and negative values and are characterized by an amplitude area close to zero. We attribute these events to electromagnetic interference with the readout apparatus. The fact that they are still detectable even when the TES is in a fully superconducting state, a condition where it is not sensitive to energy depositions, indicates that the culprit is not the TES.

*Experimental runs.* Photon-like events are the expected signal for dielectric haloscopes searching for dark matter dark photons. Therefore, it is essential to measure the intrinsic photon-like DCR in the TES (i.e., when the sensor is operated in the dark, with no optical link to ambient and in the absence of radioactive sources) as this forms the background against which the dielectric haloscope operates.

At the onset of our investigation, we expected to see an intrinsic photon-like DCR on the order of  $10^{-4}$  Hz, in line with findings by Ref. [14], the only preceding study of a similar nature. There was also a question of whether cosmic rays or natural radioactive decays, interacting with either the TES or its substrate, could account for some of these photon-like events as suggested by the same authors. To explore this possibility, and to gain a deeper understanding of the nature of high-energy events, which

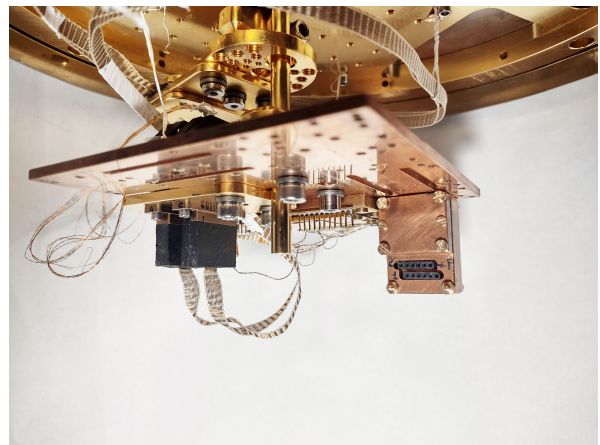


FIG. 3. The copper box containing the TESs can be seen to the right, attached to the 30 mK-stage plate. The cables for readout are disconnected in this photo.

have not been extensively studied before, we carried out four specific tests, explained below.

It is important to note that all the experimental runs were conducted in the absence of a light source and without an optical fiber connected to the TES, which was entirely encased in a copper box thermally coupled to the 30 mK-stage, as can be seen in Fig. 3. In Fig. 4, the lid of the copper box is not present and the substrates on which the TESs are deposited can be seen. Although three fibers were present in the cryostat to allow for the initial calibration procedures, their ends were fixed to the outer side of the 3 K-stage within the ADR.

The first run was a background test (Run 1) intended to measure the photon-like DCR. Additionally, in the

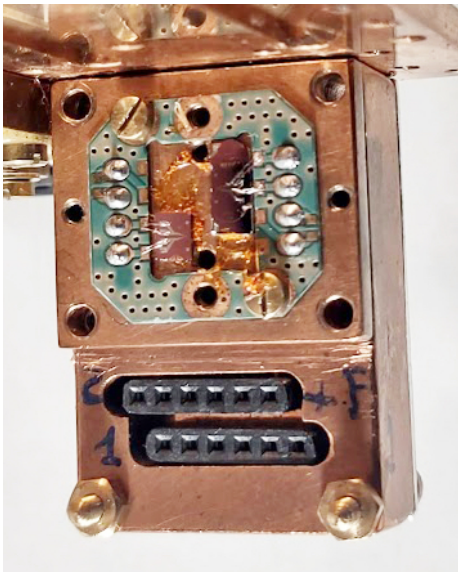


FIG. 4. Copper box housing the TESs. The lid was removed to take the photo. Although the TESs are too small to be seen, the substrates are visible with the top-right one (TES E) almost double the size of the bottom-left one (TES B).

same run, we measured the high-energy DCR, which we hypothesized to be caused by cosmic rays or natural radioactive decays interacting with the TES substrate.

In Run 2 and Run 3, we used two radioactive sources,  $^{232}\text{Th}$  and  $^{22}\text{Na}$ , respectively. These sources were placed against the exterior of the ADR and aligned perpendicularly to the TES substrate. The aim of these tests was to examine the TES's response to high-energy gamma events. In Run 2, a  $^{232}\text{Th}$  source with an activity measured at approximately 10 kBq was used. For Run 3, we employed a  $^{22}\text{Na}$  source, which had an activity of around 32 kBq. The emission spectrum of  $^{22}\text{Na}$  is characterized by two prominent photoelectric peaks. Notably, one of these peaks corresponds to the simultaneous emission of two back-to-back 511 keV photons, a phenomenon that occurs due to electron-positron annihilation following a  $\beta^+$  decay. This source was sandwiched between the ADR and a plastic scintillator connected to a PMT, which we call a “saber.” This setup allowed us to measure the double coincidences of the back-to-back gammas, capturing these occurrences with both the saber and the TES.

For the fourth test, to demonstrate that cosmic rays can induce high-energy events in the TES, we implemented a cosmic ray coincidence system, placing three sabers, side-by-side, directly below the ADR. A simultaneous triggering of the TES and all sabers indicated a cosmic ray shower or muon bundle event. The three sabers were operated at the same gain within a 10% uncertainty. The threshold was set at 120 mV on all three, which corresponds to 250 keV (see Supplemental Material for more details about the sabers' calibration [? ]).

The data acquisition was conducted in two modes: in Run 4A, which lasted about 19 hours, the oscilloscope

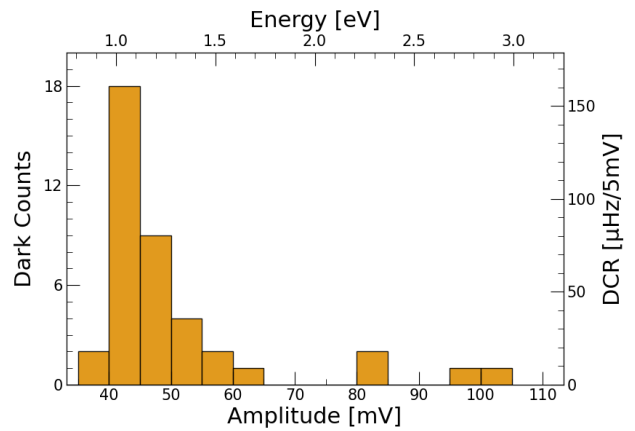


FIG. 5. Histogram of the photon-like dark counts versus amplitude (bottom x-axis) and energy (top x-axis) during the background run. 40 photon-like events were recorded over 31 hours with a trigger threshold of 0.8 eV. The right y-axis shows the rate in  $\mu\text{Hz}$  per bin.

was configured to trigger on the AND signal of the three sabers, recording the TES signal simultaneously; in Run 4B, spanning around 14 hours, the trigger was set on the TES for signals greater than 0.8 eV, while recording all three sabers' outputs. Run 4A provided the ratio of quadruple coincidences (events registered by both the TES and the three sabers) to triple coincidences (events detected solely by the sabers), while Run 4B allowed us to estimate the ratio of quadruple coincidences to the total number of high-energy events detected by the TES.

*GEANT4 simulation.* Based on preliminary calculations, it is clear that the frequency of cosmic ray interactions with the TES alone is insufficient to account for the number of high-energy events observed. This suggests that high-energy events observed by the TES originate from energy depositions within the substrate. The substrate for TES E is 6.7 mm  $\times$  2.7 mm in area and 500  $\mu\text{m}$  in thickness. We developed a GEANT4-based simulation to validate our understanding of the high-energy events seen by the sensor. We ran the simulation in three configurations named Sim 2, Sim 3, and Sim 4 which mirror the experimental setups of Run 2, Run 3, and Run 4, respectively. All simulations used the substrate as the sensitive detector rather than the TES itself.

In Sim 2, we modeled the  $^{232}\text{Th}$  source as in Run 2 and simulated one billion decay events. The simulation assumed the source to be in secular equilibrium. This approach is supported by empirical data obtained from analyzing the thorium source with a high-purity germanium (HPGe) detector at NYUAD, which provided activity level and spectral information consistent with this assumption. The activity from these measurements, around 10 kBq, was also used to convert the number of simulated decays to a time (i.e.,  $\sim 100\,000\text{s}$  for 1 billion decays).

In Sim 3, the  $^{22}\text{Na}$  source and the saber were positioned

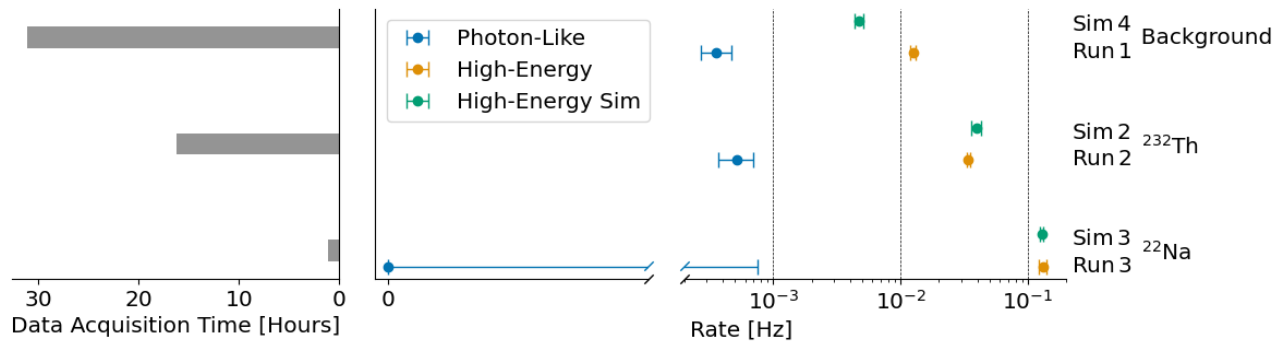


FIG. 6. TES count rates under different experimental configurations, namely when no radioactive source is present (background), with  $^{232}\text{Th}$ , and with  $^{22}\text{Na}$ . In blue are the measured photon-like rates, in orange and in green are the measured and simulated high-energy count rates, respectively. The photon-like rates could not be simulated due to their unknown origin. Background data comes from Run 1, whereas  $^{232}\text{Th}$  and  $^{22}\text{Na}$  data come from Run 2 and Run 3. The simulated high-energy event rates come from Sim 4, Sim 2, and Sim 3, corresponding to cosmic rays (which are presumed to be the predominant cause of high-energy background events),  $^{232}\text{Th}$ , and  $^{22}\text{Na}$ . As the simulations lack a built-in time, we employed various time scaling factors to convert simulation counts into rates. These factors are the triple coincidence rate from Run 4A and the activities of thorium and sodium. The uncertainties associated with each measured data point represent the 90% confidence interval from Poisson statistics. Given we observed 0 counts in Run 3, we use Feldman and Cousins [15] confidence intervals for the error bar for that data point. For the simulated rates, the errors come from propagation of uncertainty in the time scaling factors.

as in Run 3 and one billion decays were simulated. In the same way as for the thorium, we used the known activity of 32 kBq to convert the simulated number of decays to a time.

In Sim 4, we modeled the three sabers side-by-side, under the ADR, and produced ten billion secondary cosmic ray particles using the Cosmic Ray Library (CRY package [16]). These cosmic ray particles, as well as those particles produced by their interactions with the setup, hit the substrate and the sabers. The saber hits were disregarded if their energy deposition was lower than 250 keV, the trigger threshold used during data acquisition.

From Sim 4, using the triple coincidence rate from Run 4A as a time conversion factor, we obtained a simulated cosmic ray DCR. This was then compared to the high-energy DCR observed in Run 1. Additionally, Sim 4 allowed us to calculate the ratios of triple-to-quadruple coincidences and high-energy TES hits-to-quadruple coincidences. These ratios correspond to those measured in Run 4A and Run 4B, respectively.

*ICP-MS measurements.* To investigate the contribution of radioactive decays to the number of high energy events seen by the TES we conducted an inductively coupled plasma-mass spectrometry (ICP-MS) analysis at the Laboratori Nazionali del Gran Sasso (LNGS, L'Aquila, Italy). This was to evaluate the intrinsic radioactivity of the materials around the TES, specifically the substrate and the copper box housing the TES. The analysis focused on uranium and thorium, which we suspected to be the main contributors of radioactive decays. In the substrate, uranium and thorium concentrations were found to be less than 3 ppb and 7 ppb, respectively. For the copper box, concentrations of both isotopes were below 1 ppb. Upon incorporating the measured radioactivity of

the copper box and substrate into our GEANT4 simulation, it was determined that the TES would register approximately one hit every 500 days (21 nHz). This finding indicates that the impact of naturally occurring radioactivity on the high-energy DCR is negligible.

*Results and discussion.* The key finding from Run 1 is that the photon-like DCR stands at  $3.6 \times 10^{-4}$  Hz within the energy range of 0.8 to 3.2 eV. Notably, at  $1.5 \pm 0.2$  eV—the energy range targeted by the MuDHI dark photon dark matter haloscope detector—the photon-like DCR is  $6 \times 10^{-5}$  Hz. Figure 5 shows the photon-like DCR for the TES as a function of photon energy and signal amplitude.

Contrary to initial expectations, the photon-like DCR in the 0.8 to 3.2 eV energy range remained constant (within uncertainties) across all runs (see the blue points in Fig. 6), despite the introduction of radioactive sources in Run 2 and Run 3. This consistency in the photon-like DCR, regardless of the presence of radioactive sources, suggests that high-energy gammas do not contribute to the observed photon-like event rate. Despite including the Optical Physics package in our GEANT4 simulation, no optical photons indicative of scintillation processes around the TESs were recorded.

One potential explanation for the observed photon-like DCR is the presence of stray optical photons within the cryostat, possibly from external ambient light. However, the likelihood of these photons entering through the optical fiber seems minimal, as any ambient light entering the fiber would be absorbed by the 3 K-stage to which it is fixed. Supporting this, previous research indicates that the presence or absence of a fiber fed into the cryostat, but not directly coupled to the TES, has no significant effect on the photon-like DCR (see Fig. 4.13 in Ref. [17]). This suggests that the source of these photons remains

unknown and requires further investigation.

In Run 1, we also selected high-energy signals to calculate the high-energy dark count rate. This rate is considered to be caused by cosmic ray interactions with the TES substrate. Notably, for TES B, whose substrate area is half the size of TES E's, we observed that the high-energy DCR was half that of TES E, substantiating the relationship between the substrate's size and the high-energy DCR (see Supplemental Material for more details [? ]). The high-energy event rate from the cosmic ray simulation and the experimental data do not align within uncertainty. However, the rates are within the same order of magnitude. The observed discrepancies can be attributed to limitations in the CRY package, the simulation framework used for cosmic rays, and the modeling of our experimental setup.

Upon introducing radioactive sources, a noticeable increase in the rate of high-energy signals in the TES was observed on the oscilloscope. This was particularly visible with the  $^{22}\text{Na}$  source. Our simulation shows that we can accurately model the high-energy events in the presence of a radioactive source, with compatible results for both the  $^{232}\text{Th}$  and  $^{22}\text{Na}$  run. The simulation indicates that the substrate absorbs the energy and then transmits it to the TES, where it is detected. Notably, altering the substrate area linearly changes the DCR, further confirming this interaction mechanism.

Run 4 provided confirmation that cosmic ray showers are capable of producing high-energy events in the TES, as evidenced by the quadruple coincidences observed between the sensor and the three sabers below the ADR (see Fig. 7). The simulated ratio of triple coincidences to quadruple coincidences overestimates that observed in Run 4A (2337 in simulation and 477 in real life), whereas the simulated ratio of high-energy TES hits to quadruple coincidences underestimates Run 4B (198 in simulation and 321 in real life). This is likely due to the low statistics of quadruple coincidences in both runs and limitations of the cosmic ray simulation.

*Conclusions.* We have characterized the dark count rate of a Ti/Au superconducting transition-edge sensor. By employing singular-value decomposition, principal component analysis, and K-means clustering, we effectively filtered out noise and high-energy events to isolate photon-like signals. These photon-like signals are of particular interest since they resemble the expected dark photon signal in a dielectric haloscope. We achieved a photon-like DCR of  $3.6 \times 10^{-4}$  Hz in the 0.8 to 3.2 eV range. Removing optical connections between the TES and ambient is essential to achieve very low DCRs. The source of the observed residual photon-like events still remains unexplained, necessitating further investigation.

In relation to high-energy events, our runs using  $^{232}\text{Th}$  and  $^{22}\text{Na}$  sources, coupled with a comprehensive GEANT4 simulation, have allowed us to ascribe these events to high-energy depositions in the TES substrate. This marks the first time such a clear attribution has been possible. Additionally, natural radiation appears to

have a negligible impact on the TES's high-energy DCR. Instead, the primary contributor to this rate is cosmic ray particles hitting the substrate.

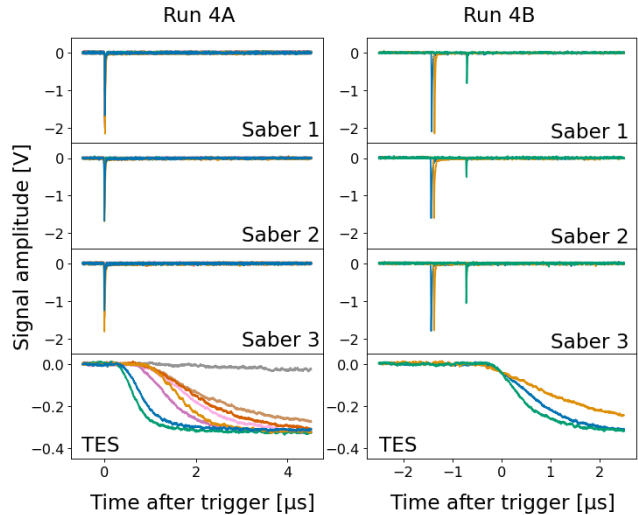


FIG. 7. Plots showing all quadruple coincidence events from Runs 4A (8 over 19 hours) and 4B (3 over 14 hours). For each simultaneous event detected across saber 1, 2, 3, and the TES, the same color is used in all four corresponding plots to represent that specific event. In Run 4A the trigger was on the AND signal of the three sabers. Due to the TES's longer, more variable rise time and delay relative to the sabers, the saber pulses appear to overlap. In Run 4B, the time window is extended to negative values to capture the saber pulses that occur prior to the TES trigger.

*Acknowledgments.* We thank Stefano Nisi and Francesco Ferella at Laboratori Nazionali del Gran Sasso (LNGS) for the ICP-MS measurements. This research was carried out on the High Performance Computing resources at New York University Abu Dhabi. We are grateful to the NYUAD Kawader Research Assistantship Program. This work was also made possible by the contribution of Grant (62313) from the John Templeton Foundation. Fermilab is operated by Fermi Research Alliance, LLC under Contract No. DE-AC02-07CH11359 with the United States Department of Energy.

## Appendix A: TES fabrication

Both TES B and TES E were fabricated at INRiM. They are composed of a 15 nm film of Ti under a 30 nm film of Au deposited on a substrate [18]. The substrate was made through low pressure chemical vapor deposition (LPCVC) and is composed of a Si substrate ( $525 \pm 25 \mu\text{m}$  thick), sandwiched between two bilayers composed of  $\text{SiN}_x$  silicon nitride (500 nm thick) and  $\text{SiO}_2$  thermal oxide (150 nm thick), with the silicon nitride as the outside layer.

The depositions were performed in a custom ultra-high vacuum (UHV) deposition chamber at a pressure less than  $5 \times 10^{-6}$  Pa, which is essential to prevent Ti oxidation and achieve a smooth interface between titanium and gold. The outline of the TESs were defined by the lift-off technique using a Heidelberg  $\mu\text{PG}101$  laser writer.

Before the deposition, the substrate underwent sputter etching for 15 seconds at 400 V. Then, the sample was moved to the UHV chamber for the Ti and Au deposition. This consisted of Ti deposition by e-beam at a rate of 0.25 nm/s followed, after about 30 s, by the deposition of Au by effusion cell at a rate of 0.07 nm/s. The deposited thicknesses were continually monitored by a quartz crystal sensor.

The wiring was made by lift-off of 50 nm of sputtered Nb. Sputter etching was used before the wiring process to reduce the contact resistance between the Nb and the TESs.

## Appendix B: Classification algorithm

To classify the event type of each waveform, we first apply a Butterworth-filter and calculate a set of variables including maximum amplitude, area, full-width at half maximum, standard deviation, average positive and negative gradient, and the cross correlation with a reference photon-like event. This gives us a point in an n-dimensional space for each TES pulse recorded by the oscilloscope.

We then perform a principal component analysis on the matrix containing the aforementioned n-dimensional points [12]. Using this technique, we can identify the two axes in this n-dimensional space that maximize variance among these points. Plotting pulses on these two axes typically results in distinct clusters. This representation enables the visual differentiation of photon-like, high-energy, and electrical noise events.

Furthermore, applying K-means clustering allows us to easily collate pulses that fall close together in the n-dimensional space [13]. The combined use of these tools, and, if necessary, reanalysis of selected pulse subgroups, enables efficient pulse shape discrimination on datasets comprised of thousands to tens of thousands of pulses in approximately ten minutes.

The software was developed in Python using the SciPy module [19] and it is available at Ref. [20].

## Appendix C: GEANT4

All code used for the simulations is available on our GitHub repository [21]. We used the GEANT4 v.11.1.2 software, an object-oriented framework written in C++ that employs Monte Carlo methods [22]. In our simulations, we activated the EmLiverMore low-energy physics module with the Particle Induced X-ray Emission (PIXE) parameter enabled.

During each simulation event, data was collected on particle characteristics, including position, initial energy, primary vertex, the sensitive volume or volumes that it hits, and the energy deposited. To simulate cosmic ray particles, which include neutrons, protons, gammas, electrons, pions, and muons, we used the Cosmic Ray Shower Library (CRY) [16].

For simulations involving thorium and sodium, we employed the Radioactive Decay module along with the General Particle Source. To optimize computing time, we limited our analysis to secondary products with a Track ID of 50 or less. We validated this approach by comparing the  $^{232}\text{Th}$  spectrum from our simulation with measurements from the High Purity Germanium detector at NYUAD (Fig. 8).

The geometry of the detector was defined using GDML files, which, when combined with macro files, allowed for the dynamic adjustment of various simulation parameters. For computationally intensive simulations, we used the Message Passing Interface (MPI) on a high-performance computer, which allowed us to use approximately 8000 CPU hours per simulation.

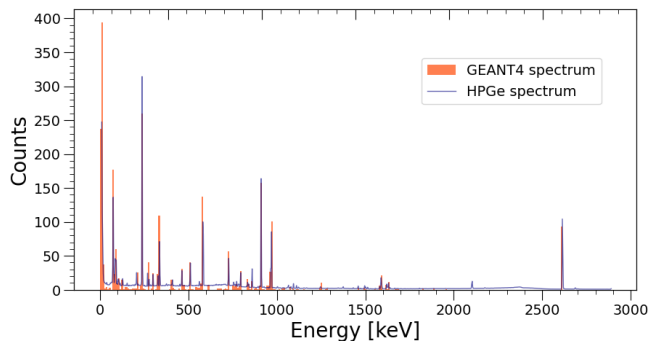


FIG. 8. Comparison of the  $^{232}\text{Th}$  spectrum: GEANT4 simulation and measurement from the HPGe detector of the thorium source. GEANT4 counts are scaled down for easy comparison with the measured counts.

## Appendix D: TES B

Figure 9 shows the energy calibration curve for TES B. A background run of 14 hours and 45 minutes resulted in 7 photon-like counts and 370 high-energy counts. The high-energy dark count rate is half that of TES E, whose substrate is twice the size of TES B's. This is consistent

with the hypothesis that high-energy events are caused by cosmic ray particle interactions within the substrate. However, the photon-like DCR is effectively the same as that of TES E, implying that the photon-like events do not originate in the substrate and as such are unaffected by the difference in substrate size.

The fact that the results from both TESs are consistent indicates that the fabrication techniques we employ are reliable and lead to reproducible sensors.

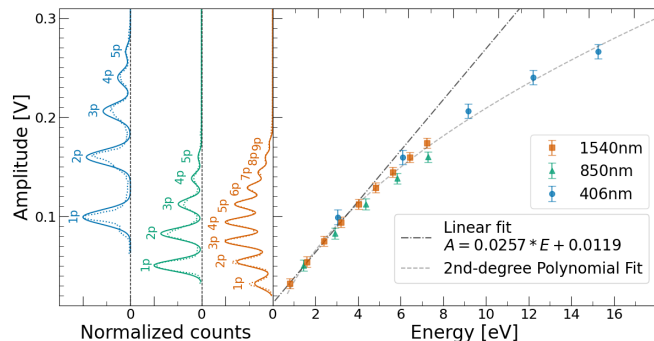


FIG. 9. Energy calibration of TES B.

### Appendix E: Sensitive volume

To assess whether the TESs were sensitive just to energy depositions in the substrate or also to energy depositions in the base of the copper box hosting them, a thorium source experiment involving both TESs was conducted. A GEANT4 simulation was also performed.

Table I summarizes our results. Both the experimental data and the simulation show comparable ratios between TES E and TES B counts, as well as similar numbers of double coincidences. These results reinforce our belief that the substrate, which is the sensitive volume in the simulation, is the only volume where energy depositions lead to detections in the TESs.

Given the base of the copper box is not a sensitive volume in the simulation, if energy deposited in the copper could be detected by the TESs in real life, we would expect the simulation to underestimate TES hits. Furthermore, since the base of the copper box connects both TESs, if the copper were able to diffuse heat to the sensors, we would observe significantly more double coincidences in real life than in simulation. Since we did not

TABLE I. Data from a thorium run with the two TESs operating simultaneously over 17.5 hours and comparison with simulation.

	TES E	TES B	Both
Experiment	687	464	7
Simulation	563	472	5



FIG. 10. GEANT4 graphic user interface output of Sim 4. It includes the ADR, the 30 mK-plate, the magnetic shield, the copper box housing the TES substrates, and, in gray, the three sabers below the refrigerator.

observe either, we conclude that energy deposited in the copper does not contribute to TES hits.

To investigate further the nature of the double coincidences, we calculated the rate of random coincidences using the formula  $N_{EB} = 2N_E N_B \cdot \frac{T}{t}$ , where  $N_{EB}$  is the number of double coincidences,  $N_E$  and  $N_B$  are the numbers of hits on TES E and TES B, respectively,  $T$  is the gate time, and  $t$  is the total measurement time. For our specific setup, which included a gate time of 100  $\mu$ s and a total time of 17.5 hours, the expected number of random double coincidences is 0.001. This number is markedly lower than the 7 occurrences we observed over the 17.5 hours. This confirms that the double coincidences are correlated and likely caused by the same initial  $^{232}\text{Th}$  decay. Through simulation, it was understood that the main source of such coincidences is secondary electrons, originating in the copper box from  $^{232}\text{Th}$  decay events, impacting the substrates simultaneously.

To further validate that the energy depositions causing the high-energy events occur only within the substrate, we conducted a series of simulations varying both the size of the substrate and its distance from the radioactive source. These simulations conform best to reality when the sensitive volume matches the real substrate size

and position and revealed a square law relationship between the count rate and the distance from the radioactive source.

## Appendix F: Saber calibration

The calibration of the sabers was carried out at NYUAD using different radioactive sources. Fig. 11 shows the calibration curve for all three sabers with the PMTs operating at similar gains.

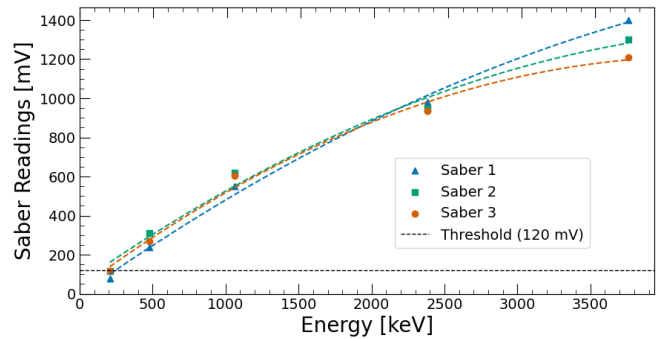


FIG. 11. Energy calibration for the three sabers at similar PMT gains. The trigger on the oscilloscope during data acquisition was set to 120 mV. The lines correspond to the second-order polynomial fits of the data points for each saber.

- 
- [1] M. Fabbrichesi, E. Gabrielli, and G. Lanfranchi, *The physics of the dark photon: a primer* (Springer, 2021).
- [2] A. J. Millar, G. G. Raffelt, J. Redondo, and F. D. Steffen, *Journal of Cosmology and Astroparticle Physics* **2017** (01), 061.
- [3] M. Baryakhtar, J. Huang, and R. Lasenby, *Physical Review D* **98**, 035006 (2018).
- [4] J. Chiles, I. Charaev, R. Lasenby, M. Baryakhtar, J. Huang, A. Roshko, G. Burton, M. Colangelo, K. Van Tilburg, A. Arvanitaki, *et al.*, *Physical Review Letters* **128**, 231802 (2022).
- [5] L. Manenti, U. Mishra, G. Bruno, H. Roberts, P. Oikonomou, R. Pasricha, I. Sarnoff, J. Weston, F. Arneodo, A. Di Giovanni, *et al.*, *Physical Review D* **105**, 052010 (2022).
- [6] C30902SH-TC-Si APD, 0.5mm, TO-66, Photon Counting, Single-Stage Cooler (2023).
- [7] J. Bienfang, T. Gerrits, P. Kuo, A. Migdall, S. Polyakov, and O. Slattery, *Single-Photon Sources and Detectors Dictionary* (2023).
- [8] K. D. Irwin and G. C. Hilton, *Cryogenic particle detection*, 63 (2005).
- [9] K. Irwin, *Applied Physics Letters* **66**, 1998 (1995).
- [10] J. M. Martinis and J. Clarke, *Journal of low temperature physics* **61**, 227 (1985).
- [11] M. Rajteri, M. Biasotti, M. Faverzani, E. Ferri, R. Filippo, F. Gatti, A. Giachero, E. Monticone, A. Nucciotti, and A. Puiu, *Journal of Low Temperature Physics* **199**, 138 (2020).
- [12] S. Wold, K. Esbensen, and P. Geladi, *Chemometrics and Intelligent Laboratory Systems* **2**, 37 (1987), proceedings of the Multivariate Statistical Workshop for Geologists and Geochemists.
- [13] D. Arthur and S. Vassilvitskii, in *ACM-SIAM Symposium on Discrete Algorithms* (2007).
- [14] J. Dreyling-Eschweiler, N. Bastidon, B. Döbrich, D. Horns, F. Januschek, and A. Lindner, *Journal of Modern Optics* **62**, 1132 (2015).
- [15] G. J. Feldman and R. D. Cousins, *Physical Review D* **57**, 3873 (1998).
- [16] C. Hagmann, D. Lange, and D. Wright, in *2007 IEEE Nuclear Science Symposium Conference Record*, Vol. 2 (2007) pp. 1143–1146.
- [17] J. Dreyling-Eschweiler, *A superconducting microcalorimeter for low-flux detection of near-infrared single photons*, Tech. Rep. (Deutsches Elektronen-Synchrotron (DESY), 2014).
- [18] E. Monticone, M. Castellino, R. Rocci, and M. Rajteri, *IEEE Transactions on Applied Superconductivity* **31**, 1 (2021).
- [19] P. Virtanen, R. Gommers, T. E. Oliphant, M. Haberland, T. Reddy, D. Cournapeau, E. Burovski, P. Peterson, W. Weckesser, J. Bright, S. J. van der Walt, M. Brett, J. Wilson, K. J. Millman, N. Mayorov, A. R. J. Nelson, E. Jones, R. Kern, E. Larson, C. J. Carey, Í. Polat, Y. Feng, E. W. Moore, J. VanderPlas, D. Laxalde, J. Perktold, R. Cimrman, I. Henriksen, E. A. Quintero, C. R. Harris, A. M. Archibald, A. H. Ribeiro, F. Pedregosa, P. van Mulbregt, and SciPy 1.0 Contributors, *Nature Methods* **17**, 261 (2020).
- [20] nyuad astroparticle: tes analysis (2024), <https://github.com/nyuad-astroparticle/tes-analysis>.
- [21] nyuad astroparticle: tes geant (2024), <https://github.com/nyuad-astroparticle/tes-geant>.
- [22] S. Agostinelli, J. Allison, K. a. Amako, J. Apostolakis, H. Araujo, P. Arce, M. Asai, D. Axen, S. Banerjee, G. Barrand, *et al.*, *Nuclear instruments and methods in physics research section A: Accelerators, Spectrometers, Detectors and Associated Equipment* **506**, 250 (2003).